





# Exploring the 3D architecture of brain tissue using digital holographic microscopy

**DENNIS SCHEIDT,<sup>1,\*</sup>  ALEJANDRO V. ARZOLA,<sup>2</sup>  LUISA DEL CARMEN GARCÍA,<sup>2</sup> CLAUDIO NARCISO RÁMIREZ,<sup>3</sup> KATRIN AMUNTS,<sup>1,4</sup> AND MARKUS AXER<sup>1,5</sup>**

<sup>1</sup>*Institute for Neuroscience and Medicine 1, Juelich Research Center, Willhelm-Johnen-Straße, Juelich, 52428, Germany*

<sup>2</sup>*Instituto de Física, Universidad Nacional Autónoma de México, C.P. 04510, Cd. de México, Mexico*

<sup>3</sup>*Instituto de Ciencias Aplicadas y Tecnología, Universidad Nacional Autónoma de México, C.P. 04510, Cd. de México, Mexico*

<sup>4</sup>*C. & O. Institute of Brain Research, Heinrich-Heine University Düsseldorf, Merowinger Platz 1a, Düsseldorf, Germany*

<sup>5</sup>*School of Mathematics and Natural Sciences, University of Wuppertal, Gausstraße, Wuppertal, Germany*  
*\*d.scheidt@fz-juelich.de*

**Abstract:** To understand the complexity of the brain, it is necessary to study its microscopic neuronal architecture and densely packed nerve fibre networks. Techniques based on histological sectioning and staining are often used for this purpose. But they can obscure or destroy valuable information and often require extensive computational post-processing for analyzing histological images. Digital holographic microscopy (DHM) enables phase and volumetric imaging. It is a promising alternative to imaging transparent biological samples with minimal preparation and high resolution. The presented study introduces DHM to image the amplitude and phase of rat brain tissue using the double-sideband (DSB) filtering technique, while reducing phase artifacts through the incorporation of unfiltered holograms into the reconstruction formalism. Combining the reconstructed complex-valued hologram with digital processing and digitally synthesized dark-field and phase contrast filtering – including the computational evaluation of light propagation and autofocusing criteria – enhances two-dimensional structural visualisation and reveals volumetric features. This approach successfully resolves the three-dimensional arrangement of crossing fibre bundles from a single acquired hologram through indirect, depth-resolved localization, which is challenging in many imaging applications. Finally, the technique is shown to be scalable, enabling full brain section scanning while supporting a compact, intrinsically multimodal imaging setup.

© 2026 Optica Publishing Group under the terms of the [Optica Open Access Publishing Agreement](#)

## 1. Introduction

Mammalian brains consist of several millions to hundreds of billions of neurons, such as the human brain. Each neuron is connected to up to 10,000 other neurons via synapses, making the brain networks highly complex [1]. To understand network function and ultimately the emanating behaviour, a multiscale description encompassing the molecular, cellular, and macroscopic levels is required [1,2]. Spatial reconstruction of both local and long-distance neural networks is a key goal, but yet one of the most challenging due to the densely and complexly interwoven nerve fibers (i.e., the threadlike projections of myelinated and non-myelinated axons) whose signals are difficult to disentangle. Depending on the scale and on the aspects of interest, various neuroimaging methodologies have been developed over recent years. The subcellular level, for instance, can be studied using Electron Microscopy, which allows resolving individual neurons and their closest connected neighbors within a few cubic millimetres at nanometer resolution [3,4]. Magnetic Resonance Imaging (MRI) is the primary technique used to study the whole

brain at a macroscopic level, reaching a resolution at the submillimeter range that that allows to model prominent long-distance fiber pathways [5,6].

Optical microscopy is the preferred choice for examining brain architecture at the cellular level, i.e. at the (sub-) micro-meter scale [7–10]. At this scale the brain's intricate communication networks building projection, association and commissural fiber pathways can basically be addressed beyond current MRI capabilities. However, deep white matter pathways and cortical connections, for example, challenge complementary microscopy techniques differently due to the networks' hierarchical, multi-scale nature [1].

This work combines and integrates established holography techniques in a digital holographic microscope to show that double sideband filtering based holography is a powerful, efficient, and scalable method for full sample measurements label-free 3D tissue imaging of 50 – 100 $\mu\text{m}$  thick samples. It holds promise for advancing histological analysis, especially in resolving complex fiber structures, either on its own or alongside compatible techniques using the same tissue preparation.

A large number of optical methods rely on bright-field microscopy and histological staining to visualize neurons, myelinated axons or non-myelinated axonal projections. However, staining always comes with the limitation of randomly targeted or unspecific locations, and these labelled sections require extensive manual preparation prior to scanning as well as specific stains to reveal particular structures [11,12]. Correlative imaging, i.e. the use of different contrast mechanisms in the same tissue sample, may overcome such challenges. In particular, the combination of label-free approaches appear to be appealing in this context. However, combining different modalities typically requires measurements in separate optical setups, necessitating image registration. This can be challenging, as landmarks may exhibit different contrast across modalities and the optical field can be distorted by the imaging optics, thus often requiring complex and computationally intensive nonlinear registration algorithms [13].

Commonly used label-free imaging techniques are dark-field microscopy [14] and phase-contrast microscopy [15,16] offering improved contrast over bright-field microscopy. These techniques add amplitude or phase modulation to the Fourier plane of the transmitted light to increase the contrast of the acquired images. They find applications in highly transparent samples, such as biological tissues or cell cultures. Specialized label-free imaging techniques, such as Polarized Light Imaging (3D-PLI) [9] and Scattered Light Imaging (SLI) [17], are sensitive to specific tissue components, such as myelin and nerve fibers, due to optical birefringence or anisotropic light scattering, respectively. 3D-PLI and SLI are effective at mapping the 3D nerve fiber architecture from 2D measurements at the microscopic level. These methods measure 2D projections of the 3D nerve fiber courses, where the accumulated signal represents the total light interaction along its propagation path, which limits the visualization capabilities of complex fiber constellations across the entire depth of the brain sections. In particular, crossing fibers are a common challenge in brain imaging, including diffusion MRI, where tractography algorithms attempt to infer fiber pathways to map connectivity between brain areas at the microscale [18,19]. Therefore, microscopic techniques capable of resolving crossing fibers could provide critical data to improve these tractography algorithms.

Holography is a promising approach to remove the general limitation of 2D projection analysis and complement the micro-structural characterization based on 3D-PLI and SLI, for example. Holography captures the amplitude and phase distribution of the field distorted by the the object of interest, allowing volumetric analysis from a single 2D image. Applications include quantitative phase measurements [20,21], particularly for characterizing biological objects [20,22], and even *in-vivo* blood flow measurements due to high acquisition rates [23]. In addition, digital reconstruction of the entire 3D light field is possible through computational propagation [24]. This type of propagation has been widely used, for example, in *in-vitro* imaging of moving bacteria [25,26], 3D cell reconstruction [27,28], and image segmentation [29]. However, to

the best of our knowledge, its application to histological data has not been attempted because DHM traditionally requires optically thin samples with minimal scattering and limited wavefront distortion. Furthermore, as holography yields the reconstructed amplitude and phase of the light field, digital filtering can be implemented to mimic dark field or phase contrast microscopy, enhancing features of interest. While human brain samples have been analyzed using dark-field [30] and qualitative phase-contrast microscopy [31], these methods rely on analog apertures that modulate the retardation using an SLM rather than performing these modifications digitally [32,33]. Advanced holographic imaging techniques, such as holographic tomography [34], achieve very high resolution but are limited to small areas of a few micrometers and are impractical for large-scale imaging due to lengthy measurement times and data storage requirements [34].

Various application-specific configurations of DHM have been proposed to accurately retrieve the phase and the amplitude of the light field [35]. In particular, approaches based on in-line holography have proven to be robust, simple and accurate, and have found a wide range of applications in biology [20]. These approaches are based on the idea that the reference and modulated fields travel along the same optical path, thus avoiding mechanical and thermal instabilities for long-term experiments and allowing their implementation in standard incoherent light optical microscopes [36–38]. One such technique is the Double Side Band (DSB) filtering method introduced by Rámirez et al [39]. In this method, two holograms are acquired, each containing only half of the Fourier spectrum of the transmitted light field. This filtering separates the Fourier spectrum, so that the virtual twin image can be canceled when the two holograms are combined after applying the opposite sideband filter digitally to each hologram.

Building on the approach of Rámirez et al. [39], a microscope with sideband filters was implemented using a spatial light modulator (SLM), while simplifying the optical setup to minimize components and improve usability for non-expert users. Reducing the degrees of freedom required for operation increased the robustness of the experimental setup, particularly for microscopy applications. The resulting holograms, free of the virtual twin image, represent the transmitted light field as complex numbers, encoding both amplitude and phase. These amplitude and phase images of brain tissue provide label-free insight into the underlying structure, distinguishing features such as blood vessels, fibers, and larger bundles of fibers.

This article first introduces the concept of DSB holography as an application of digital holographic microscopy for thick, dense tissue samples, such as brain tissue. Secondly, the acquired holograms are analyzed to retrieve the phase and amplitude distributions of the transmitted light through the sample. In addition, digital filtering techniques are applied to extract dark-field and phase-contrast images from the original holograms without loss of information, avoiding measurements in separate setups and eliminating the need for image registration across different modalities, thereby enabling a straightforward multi-modal approach for tissue analysis. Thirdly, the sample volume is computationally reconstructed from a single 2D hologram via wavefront propagation, providing access to the three-dimensional spatial structure of the specimen without the need for additional measurements or assumptions. By applying autofocus criteria to the propagated volume, crossing fiber structures are resolved by determining the axial positions of fiber bundles, addressing one of the major challenges in optical measurements of brain tissue for connectivity studies. Finally, the scalability of the measurement process is demonstrated, enabling the efficient analysis of entire sections of biological samples.

## 2. Methods

A schematic of the experimental setup is shown in Fig. 1(A). A lens pair, L1 and L2 ( $f_1 = f_2 = 3$  cm), generates a 1:1 image of the LED active area (emission at the wavelength  $\lambda = 625$  nm with 17 nm bandwidth) in a  $4f$  configuration. A pinhole ( $d = 50$   $\mu$ m) is placed at the focal spot to act as a spatial low-pass filter. The pinhole size determines a trade-off between wavefront quality and illumination power: a smaller pinhole improves planar wavefront quality at the cost of reduced light

intensity. The filtered light, collimated by lens L3 ( $f_3 = 10$  cm), produces a nearly planar wavefront with spatial coherence  $L_{spatial} = \frac{\lambda}{\theta}$ , where  $\theta$  is the angular size of the light source. Here, the angular size of the transmitted light cone is  $\theta = \arctan(d/f_3) \approx 0.03^\circ$ , yielding  $L_{spatial} \approx 1.3$  mm. Temporal coherence is increased by introducing a band-pass filter ( $\lambda_0 = 633$  nm,  $\Delta\lambda = 6$  nm), achieving a coherence length of approximately  $L_{temporal} = \frac{\lambda^2}{\Delta\lambda} \approx 66.8\mu\text{m}$ .

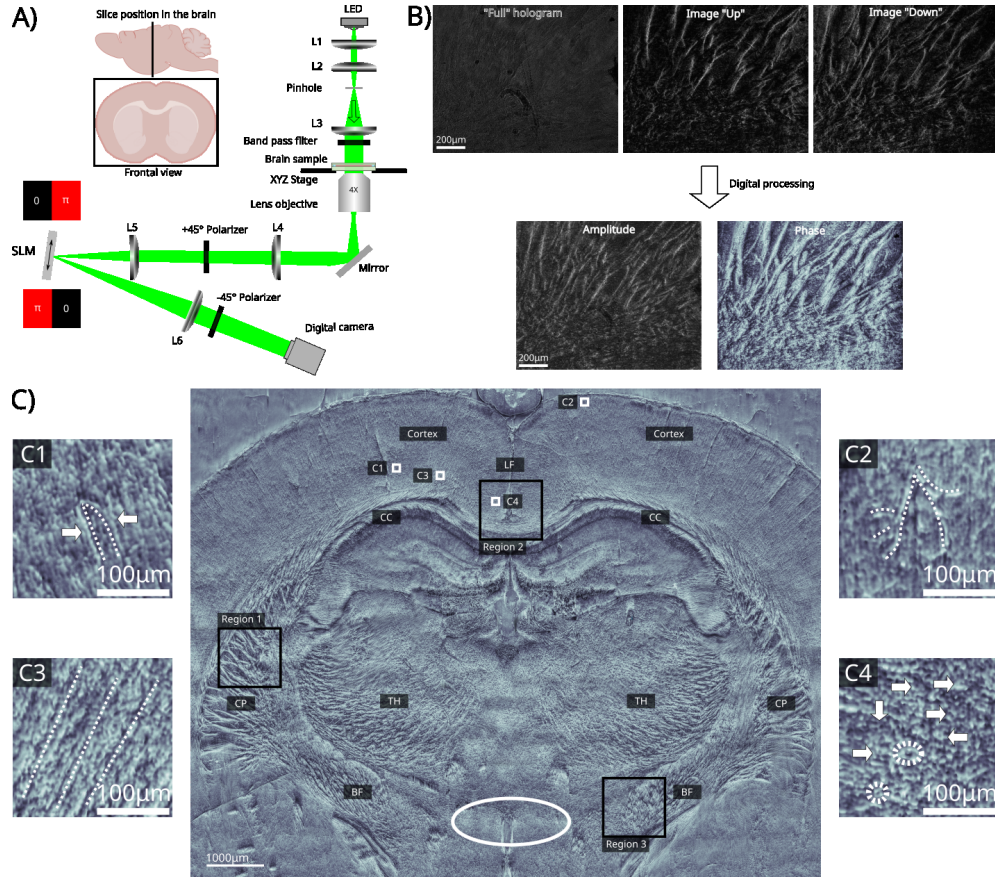


**Fig. 1.** Digital Holographic Microscopy of brain tissue. **A:** Schematic of the microscope based on the DSB with an SLM. The SLM located in the Fourier plane and in between the two polarizers at  $+45^\circ$  and  $-45^\circ$  allows to obtain a sequence of three holograms ( $I_+$ ,  $I_-$ ,  $I_{full}$ ) corresponding to three different configurations in the modulation of the spectrum: (i) upper half blocked (ii) lower half blocked and (iii) no modulation. The first polarizer prepares the light to a  $+45^\circ$  polarization state. The SLM rotates the polarization state of one sideband by  $90^\circ$  by applying a phase offset of  $\pi$ , while the other sideband is not modulated. Only the modulated polarization component passes through the second polarizer. **B:** Acquired holograms and resulting amplitude and phase of a single region. The "full" hologram does not show many features of the tissue that are only visible in the "+" and "-" images. These structures are then visible in the reconstructed amplitude and phase image. **C:** Stitched, composed phase image of the entire section. CC: Corpus Callosum, LF: Longitudinal Fissure, CP: Caudate Putamen, TH: Thalamus, BF: Basal Forebrain White ellipses show artifacts caused by the stitching algorithm. Figures C1 and C2 show blood vessels, C3 nerve fibers with their outlines highlighted by dashed white lines. Figure C4 shows neurons indicated by white dashed ellipses. White arrows indicate structure boundaries. A high-resolution image is provided as a supplement [40] and as [Visualization 1](#).

The coherent light illuminates the sample (brain tissue), placed on a manual XYZ stage. A 4× objective lens (Olympus,  $NA = 0.1$ ), combined with lens L4 ( $D = 5.08$  cm,  $f_4 = 20$  cm) provides an effective transverse magnification of  $M_T = 4.58$ . The light is then passed through a linear polarizer, set to  $+45^\circ$ , and focused by lens L5 ( $f_5 = 10$  cm) onto the surface of the Spatial Light Modulator (SLM). Lens L5 is mounted on a linear micrometer stage for precise positioning of the focal point.

A Spatial Light Modulator (SLM, Meadowlark, pixel size:  $8\mu\text{m}$ ) is used to implement Double Side Band (DSB) filtering, where half of the Fourier spectrum is selectively blocked by applying two phase retardations to each half of the SLM screen. The SLM is precisely positioned using the knife-edge method, assisted by a motorized linear stage with a resolution of  $1\mu\text{m}$ . The SLM applies a phase retardation of  $\pi$  (or  $180^\circ$ ) to the horizontally polarized component of a sideband, while leaving the vertical polarization unmodulated. This results in a  $90^\circ$  rotation of the polarization vector in the modulated sideband. After the SLM, the beam is recollimated with lens L6 ( $f_6 = 10$  cm) and the light field is imaged onto a digital camera (Basler ace, pixel size:  $\Delta x = 4.9\mu\text{m}$ ). Lenses L5 and L6 form a 4f setup, with the SLM positioned at the Fourier plane for spatial filtering. A second polarizer, oriented at  $135^\circ$ , is placed between L6 and the camera. This polarizer selectively blocks the light that has not undergone the phase shift, ensuring that only the modulated component contributes to the final image. The spatial resolution of the setup is  $2.76\mu\text{m}$  determined with the USAF test target.

The samples used are rat brain sections (*Rattus norvegicus*) of  $100\mu\text{m}$  thickness. The brains were extracted post mortem, frozen, and sectioned using a cryomicrotome. Sections were then fixed in a 20% glycerol-water solution and mounted between specimen and coverslips. Sections were cut along the coronal plane. Detailed preparation protocols are described in [41].

Three images were acquired for each measurement (Fig. 1(B)): 1.  $I_+$ , which samples the left sideband by applying a  $\pi$  phase shift to one half of the SLM, leaving the other half unmodulated. 2.  $I_-$ , which samples the other sideband with inverted SLM modulation. 3.  $I_{full}$ , an unfiltered hologram, obtained by applying a  $\pi$  phase shift to the entire SLM screen. Note, that the contrast in this image is poor, while the DSB filtered holograms show clear tissue features. Each image is acquired with an exposure time of  $t_{exp} = 200\text{ms}$  and an SLM update rate of 15Hz, so that a single region is measured with one second.

By applying inverse sideband filters to  $I_+$  and  $I_-$  in the Fourier domain and combining the resulting images, the complex light field  $U$  is reconstructed. The amplitude and phase distributions are obtained by taking the absolute value and the argument of  $U$ , respectively, as shown in Fig. 1(B). A detailed derivation of this reconstruction process is presented in the following Section. The amplitude and phase images for each region are then combined using a stitching algorithm [42] to reconstruct the images for the entire sample section as shown in Fig. 1(C).

Unlike intensity-based images, where Fourier-domain filtering operates only the magnitude and discards phase information, the reconstructed complex light field  $U$  contains both amplitude and phase. This allows the application of digital filters to achieve different imaging modalities without additional optical components [15,31,32].

For dark-field microscopy, zero-order frequency components in the Fourier spectrum of  $U$  are blocked. For phase-contrast microscopy, a  $m\pi$  phase shift is applied to the zero-order component, corresponding to a retardation of  $\Gamma = m\lambda/2$ , where  $m \in [0, 2]$ . These operations enhance contrast without altering or losing the underlying structural information, similar to the approach of [33].

The full light field reconstruction also allows the simulation of light propagation through the sample, to visualize 3D structures with submicron axial resolution using scalar diffraction theory. Notice that the propagation of the light field enables a substantially higher axial resolution compared to the optical resolution. The optical resolution is limited by the Numerical Aperture (NA) of the optical system, given by  $\Delta z_{optical} = \frac{2\lambda}{NA^2}$ , and for the microscope used, this corresponds to  $\Delta z_{optical} = 104\mu\text{m}$ . In theory, the axial resolution achievable through propagation is arbitrary.

In practise, it is determined by the ability to resolve phase differences in the holograms [43,35], which are set by the resolution of the optical path difference (OPD =  $\Delta n \Delta z$  [44]) between two points at different axial positions:  $\Delta \phi = 2\pi / \lambda \text{OPD}$  [45]. Accordingly, the phase resolution  $\sigma_\phi$  of the optical system limits the axial resolution according to  $\Delta z_{\text{prop}} = \frac{\lambda}{2\pi \Delta n} \sigma_\phi$ . Noise measurements in the imaging setup yield a phase noise of 0.06 radians, resulting in an axial resolution of 200nm. Phase-based axial localization performance was evaluated by localizing isolated PDMS beads in an aqueous solution. In thick, heterogeneous tissue samples, multiple scattering, phase mixing, and overlapping structures limit the ability to resolve closely spaced features along the axial direction. Therefore, the theoretical axial resolution does not directly translate to dense samples. Taking these effects into account, as well as phase artifacts introduced by the DSB filtering technique, an effective axial localization precision of  $z_{\text{prop}} \approx 1 \mu\text{m}$  is estimated.

Details on the computational implementation of the digital filtering and light field propagation can be found in Sections 4 and 5 of the [Supplement 1](#).

### 3. Reconstruction of the wavefront using DSB

The spectrum of the 100  $\mu\text{m}$ -thick rat brain sample is not significantly different from the case of an empty sample. This is due to the fact that the power spectrum of our sample is a perturbation of the free power spectrum, as shown in Fig. 1 in the [Supplement 1](#). The central peak corresponding to  $U_0$  is slightly reduced due to increased scattering and absorption, but a substantial fraction of the light remains unperturbed. The perturbations of the field caused by scattering form the sample field  $\Delta U$ , which is represented by the higher frequency terms in the spectrum. Thus, despite the complexity of the tissue sample, the spectral representation of the hologram still allows decomposition into the unperturbed field  $U_0$  and the sample field  $\Delta U$  (see [Supplement 1](#), Fig. 1).

Therefore, the traversing sample field can be described by the superposition  $U = U_0 + \Delta U$ . In particular,  $\Delta U$  has the form:

$$\Delta U(x, y) = U_0 t(x, y) \exp(i\phi(x, y)) . \quad (1)$$

Where  $U_0$  is the amplitude of the illumination field,  $t(x, y)$  is the amplitude transmittance and  $\phi(x, y)$  is the phase delay. In particular,  $t \in [0, 1]$  represents the amount of light that is absorbed while the field is being transmitted through the sample according to the generalized Lambert-Beer law,

$$t(x, y) = \exp(-\mu_{\text{tot}}(x, y)\Delta z(x, y)) , \quad (2)$$

Where  $\mu_{\text{tot}} = \mu_{\text{abs}} + \mu_{\text{scat}}$  is the total attenuation coefficient from absorption and scattering,  $\Delta z$  is the thickness of the sample which is assumed to be constant all along the sample. The acquired phase  $\phi$  is expressed as

$$\phi(x, y) = \frac{2\pi}{\lambda} \Delta z(x, y)(n_m - n_s(x, y)) , \quad (3)$$

where  $n_m$  and  $n_s$  are the refractive indices of the medium and the sample, respectively.

A hologram acquired close to the sample plane  $I_{\text{full}}$  thus reads as

$$I_{\text{full}} = |U_0 + \Delta U|^2 = I_0 + \Delta I + 2\sqrt{I_0 \Delta I} \cos(\Delta\Phi) ,$$

where  $I_0 = |U_0|^2$  and  $\Delta I = I_0 t^2$  are the intensities of the illuminating and of the scattering fields, respectively.  $\Delta\Phi = \phi_0 - \phi$  is the accumulated phase delay between the two wavefronts. This acquired holographic intensity pattern  $I_{\text{full}}$  is proportional to the transmission function of the tissue, but does not provide any information about the amplitude and phase of the sample field

$\Delta U$ . In particular, based on the DSB method, the amplitude and phase of the sample field  $\Delta U$  can be calculated from  $I_+$  and  $I_-$  as follows [46](see Supplement 1 section 2 for details):

$$U_{DSB} = \mathcal{F}^{-1}\{\mathcal{F}\{I_+\}u_- + \mathcal{F}\{I_-\}u_+\}, \quad (4)$$

where  $u_+$  and  $u_-$  are the digital implemented side band filters of opposite sign. The side band filter is similar to applying a Hilbert transform  $H$ , so that the DSB signal reads:

$$U_{DSB} = \frac{1}{4}(I_0 + 2U_0\Delta U^* + |\Delta U|^2 + |H(\Delta U)|^2) - iR, \quad (5)$$

where  $R = (H(\Delta U_r)H(\Delta U_i) - H(\Delta U_i)H(\Delta U_r))$ . Here,  $\Delta U_r$  and  $\Delta U_i$  are the real and imaginary parts of the sample light field and  $|H(\Delta U)|^2$  is the magnitude of the Hilbert transform of the sample light field. We also define  $U'_{DSB} = \mathcal{F}^{-1}\{\mathcal{F}\{I_+\}u_+ + \mathcal{F}\{I_-\}u_-\}$ . Starting from Eq. (5), introducing  $U_+ = U_{DSB} + U'_{DSB}$  and  $U_- = U_{DSB} - U'_{DSB}$  and using the full hologram  $I_{full}$ , the signals can be combined to cancel out some effects of the Hilbert transform via  $U_{DSB,opt} = U_{DSB} - \frac{1}{2}\Re\{U_-\} - (U_+ - \frac{1}{2}I_{full})$ , which results in:

$$U_{DSB,opt} = \frac{I_0 + \Delta I + 2U_0\Delta U^*}{4} + iR. \quad (6)$$

This signal is computed using digitally implemented filter functions  $u_{\pm}$ , with the Fourier transforms  $\mathcal{F}$  evaluated via an FFT implementation. Details of their implementation can be found in the Supplement 1, section 3.

Furthermore, the Hilbert transforms of the real and imaginary parts of  $\Delta U$  are:

$$H(\Delta U_i)H(\Delta U_r) = H(U_0t \sin \Delta\Phi H(U_0t_S \cos \Delta\Phi)) \quad (7)$$

$$= I_0H(t \sin \Delta\Phi H(t \cos \Delta\Phi)) = aI_0 \quad (8)$$

$$H(\Delta U_r)H(\Delta U_i) = H(U_0t \cos \Delta\Phi H(U_0t \sin \Delta\Phi)) \quad (9)$$

$$= I_0H(t \cos \Delta\Phi H(t \sin \Delta\Phi)) = bI_0 \quad (10)$$

These expressions cannot be further simplified without making assumptions about  $t$  or  $\Delta\Phi$  and are therefore denoted as  $a$  and  $b$ . Note, that the Hilbert transform is closely related to the gradient along the  $x$ -direction [47]. Therefore, the spatial derivatives of the amplitude  $\partial_x(t)$  and the phase  $\partial_x(\Delta\Phi)$  determine the strength of the terms  $a$  and  $b$ .

In the case of thin tissue samples, the modulation of amplitude and phase have the same origin, while the modulation of amplitude is assumed to be small. Furthermore, the thickness  $\Delta z$  can be assumed to be constant or only slightly varying and  $\mu(x, y) \ll 1$ . Consequently,  $t \approx 1$ ,  $\partial_x(t) \ll 1$ ,  $\Delta\Phi \in [0, 2\pi]$  and  $\partial_x(\Delta\Phi) \ll 1$ . Tissue is a strongly heterogeneous medium, where different tissue structures have strongly varying optical properties, but in the center of such structures the variations of  $\Delta\Phi$  are small, so that the Hilbert transforms  $a$  and  $b$  vanish. Thus, the measured amplitude and phase can be expressed as:

$$|U_{DSB,opt}| \approx \frac{I_0}{4} \sqrt{1 + 6t^2 + t^4 + (4 \cos(\Delta\phi))t(1 + t^2)} \quad (11)$$

$$\arg(U_{DSB,opt}) \approx \arctan 2 \left( \frac{\sin(\Delta\Phi)}{1 + \cos(\Delta\Phi)} \right) = \frac{\Delta\Phi}{2} \quad (12)$$

This implies that the measured amplitude signal includes contributions from both amplitude (defined by the transmission function  $t$ ) and phase modulation, while the measured phase is scaled by a factor of 2.

Approximating expression **11** and assuming without loss of generality, that  $\phi_0 = \text{const.} = 0$ ,  $t$  and  $\Delta\Phi$  can be determined as  $\phi = 2 \arg(U_{DSB_{opt}})$  and  $t = |U_{DSB_{opt}}|/2 \cos(\phi)$ . Since  $\phi$  is approximated, dividing by  $\cos(\phi)$  can introduce significant error. To obtain a more robust approximation, it is assumed that the variations in  $\Delta\Phi$  are small, which allows the approximation  $\cos(\phi) \approx 1$ . This simplifies to  $t \approx \sqrt{|U_{DSB_{opt}}|} - 1$ .

As a result, the attenuation coefficient  $\mu_{tot}$  and the refractive index  $n_s$  can be calculated using Eqs. (2) and (3):

$$\mu_{tot} \approx \frac{-\ln\left(\sqrt{|U_{DSB_{opt}}|} - 1\right)}{\Delta z} \quad (13)$$

$$n_s \approx n_m + \frac{\lambda \arg(U_{DSB_{opt}})}{\pi \Delta z}. \quad (14)$$

## 4. Results

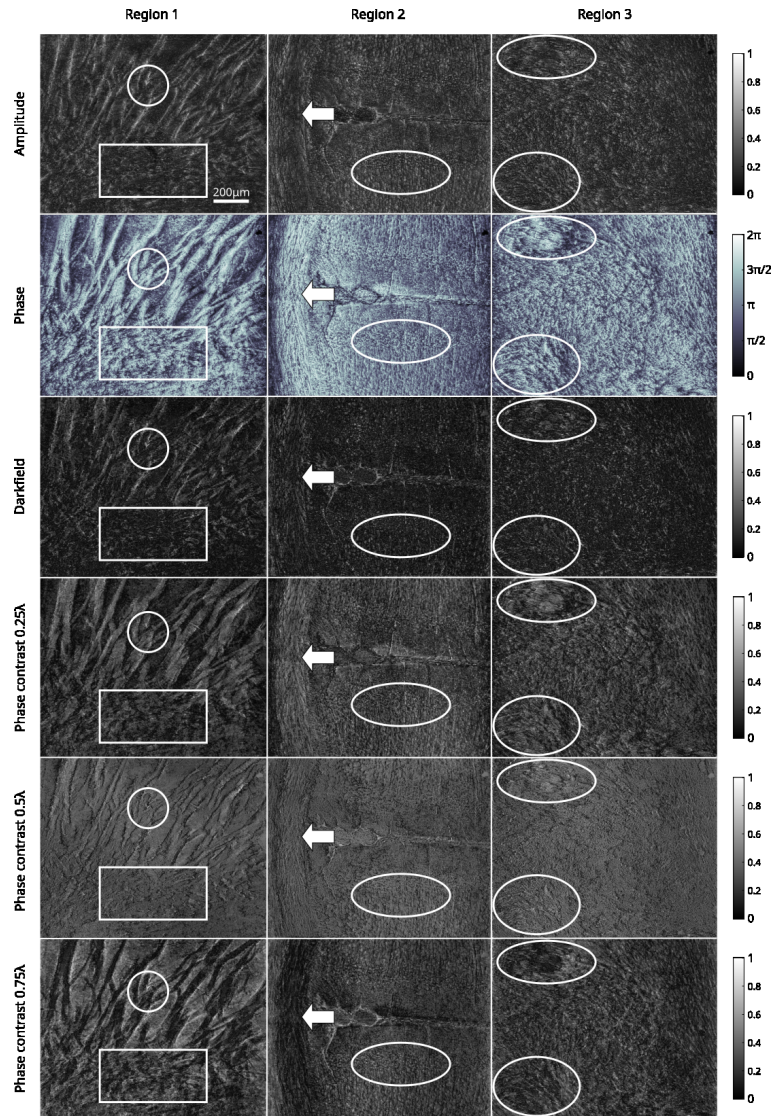
### 4.1. Unrevealing microscopy structures from the DSB holograms

Figure 1(C). shows the reconstructed phase of a 100  $\mu\text{m}$  thick and approximately  $2 \times 1$  cm section of the rat brain sample. The section was imaged by manually scanning the sample in a  $22 \times 10$  grid, with each image consisting of  $1024 \times 1280$  pixels, corresponding to an area of  $1.1 \times 1.4$   $\text{mm}^2$ . The stitching algorithm provided by Fiji [42] was then used to combine the individual images into a single composite image of the entire section. Note, that the overlap between the individual images is inconsistent, causing difficulties for the stitching algorithm and resulting in artifacts at the specimen boundaries. These artifacts appear as "wave-like" distortions (indicated by white ellipses) where the images could not be perfectly aligned. However, these artifacts affect less than 5% of the specimen, primarily at the intersections of overlapping images, leaving the overall structure of the entire section largely unaffected.

Unlike brightfield microscopy, which provides low contrast for different tissue components, the reconstructed phase shows clear distinctions between blood vessels (Fig. 1(C1) and (C2)), radially oriented nerve fibers (Fig. 1(C3)) from the Corona Radiata and neurons (Fig. 1(C4)) from layers III and IV of the cingulate cortex. Dashed white lines and white arrows indicate the outlines of the blood vessels and nerve fibers in C1-C3. Dashed circles and white arrows indicate the position of neuronal cell bodies, which can be identified as dark dots. Structures have been cross-checked with transmittance images obtained by 3D-PLI. The cortical regions with a high density of neuronal cell bodies appear homogeneous, while heterogeneous regions with large nerve fibers are easily distinguished. Such distinguishable fiber structures are: the Corpus callosum (CC), which connects the two brain hemispheres; the Caudate Putamen (CP), characterized by radial fibers extending from the center of the brain toward the cortex; and the Thalamus (TH) and Basal Forebrain (BF), where the nerve fibers pass into the image plane. These structures were identified using the EBRAINS Waxholm Rat Atlas (RRID: SCR\_017124) [48].

To highlight these different cellular structures in more detail, three regions were selected from Fig. 1(C)) and are displayed in Fig. 2. Each image shown is the original acquired image without any additional post-processing (such as stitching).

The reconstructed amplitude images in the first row of Fig. 2 provide high contrast at the boundaries of different tissue structures, regardless of the region. This effect is particularly evident in Region 1, where the thick fiber bundles exhibit a well-defined bright outline. In regions such as the cortex near to the hemispheric fissure that contains more cellular structures compared to white matter (Region 2), the outlines of neurons and blood vessels are clearly visible, appearing as circular and worm-like structures, respectively. In regions where numerous fibers



**Fig. 2.** Different digital holographic microscopy modalities (organized in the rows) for three regions (in the columns) selected from Fig. 1(C). The columns represent the three different regions, while the rows show different digital modalities in the following order: amplitude and phase of the DSB hologram, followed by digitally applied dark field and phase contrast to the amplitude image with phase shifts of  $\lambda/4$ ,  $\lambda/2$ , and  $3\lambda/4$ . Region 1 contains mainly thick, radial fiber bundles from the left Caudate Putamen. Region 2 represents the hemispheric fissure near the Corpus Callosum. Region 3 is taken from the basal forebrain and shows fibers inclined out of the imaging plane. The circle in region 1 marks a fiber crossing, the rectangle highlights a heterogeneous region of inclined fibers and cell bodies. The arrow in region 2 marks the in-plane nerve fiber bundle forming the Corpus Callosum and the white ellipse shows a region of the cortex just below the hemispheric fissure. Region 3 contains several out-of plane fibers, that appear as islands highlighted by white ellipses. A high-resolution image is provided as [Visualization 2](#).

are oriented out of the sample plane and fiber crossings are abundant distinguishing specific structures becomes much more challenging (Region 3).

The phase images in the second row provide much higher contrast and much more information compared to the amplitude images. In Region 1, instead of just outlining the nerve fiber bundles, the entire 3D structure becomes visible. In particular, the image shows that some nerve fibers lie on top of or underneath others, allowing the resolution of fiber crossings, which are typically challenging to resolve (indicated by the white circle). In addition, the lower portion of the phase image (marked by the white rectangle) reveals numerous crossing structures that are invisible in the amplitude image. In the cortex and the hemispheric fissure (Region 2), a 3D relief of individual neurons is visible (compare to Fig. 1(C4)), allowing a much clearer distinction between different tissue compartments (white ellipses). In particular, the nerve fibers of the Corpus Callosum (white arrow) appear elevated compared to the surrounding cortical region near the hemispheric fissure. This effect is even more pronounced in Region 3, where inclined or out-of-plane fibers dominate. In these regions, the amplitude images show only scattered white spots, while the phase images reveal clear details. In particular, elevated "islands" corresponding to out-of-plane fibers are visible (white ellipse).

The third row of Fig. 2 shows the amplitude of the digitally implemented dark field. Compared to the amplitude of the DSB hologram, the contrast is significantly improved, making it easier to distinguish the boundaries between different structures.

Finally, rows 4 through 6 display amplitude images with digitally applied phase contrast using retardance values of  $0.25\lambda$ ,  $0.5\lambda$ , and  $0.75\lambda$ , respectively. At first glance, these images appear to contain the same structural information but with varying contrast and gray values. Focusing on Row 4, it becomes clear that features that were only visible in the phase images are now visible in the amplitude of the phase contrast images. This is especially true for fiber structures, such as the in-plane radial fibers in Region 1 and the out-of-plane inclined fibers in Region 3.

The attenuation coefficient  $\mu_{tot}$  and the refractive index  $n_s$  can be derived from the DSB holograms using Eqs. (14) and (14). The corresponding maps for the three regions shown in Fig. 2 are presented in Fig. 3. Before computing the refractive index maps, a phase unwrapping algorithm [49] was applied, following an approach similar to [50]. For the computation of the attenuation coefficient and the refractive index, a constant  $\Delta z = 100 \mu\text{m}$  was assumed for each single image and  $n_m = 1.36$  was calculated for a 20% water-glycerol solution.

#### 4.2. Identifying volumetric structures with auto-focusing

The light field  $U_{DSB}$  was propagated in steps of  $\Delta z = 1 \mu\text{m}$  for a total distance of  $z = 50 \mu\text{m}$  in both positive and negative directions from the focal plane, covering the full thickness of the tissue section ( $d = 100 \mu\text{m}$ ). This propagation assumes that the focal plane of the microscope is positioned near the central thickness of the specimen at  $z_0 = 50 \mu\text{m}$ , which is set as the reference point ( $z_0 = 0$ ). A negative propagation direction is toward the microscope objective (i.e. toward the top of the sample), while a positive propagation direction is toward the SLM (i.e., toward the bottom of the sample). In addition to the sample light field  $\Delta U$ , the phase contrast images with  $\Gamma = 1/8, 1/4, 1/2, 3/8, 1/2$  and  $3/4\lambda$  are calculated at each propagated plane. Figure 4 illustrates the light field propagation in Region 1 of Fig. 2. **Visualization 4** and **Visualization 5** show videos of the propagated amplitude and applied phase contrast of  $\Gamma = 1/4$  over the full distance from  $[-50, 50]\mu\text{m}$ .

Propagation of the initial hologram through these axial  $z$ -planes reveals local changes in the tissue structures, which sharpen and change shape at different focal planes. To demonstrate this behavior, two regions of crossing fiber bundles composed of numerous single axon fibers are selected. The first (Fig. 4(A)) extends over sized  $200 \times 200$  pixels and features three overlapping fiber bundles. The second (Fig. 4(C)) has a size of  $160 \times 160$  pixels and features two crossing fiber bundles that are close to a third fiber bundle. For all images of the two regions the Tamura

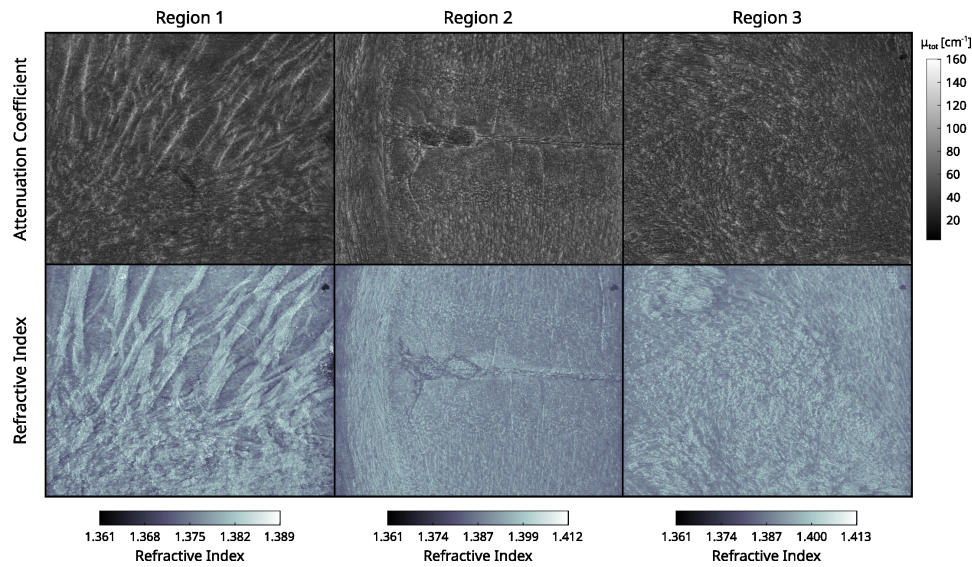


**Fig. 3.** Attenuation coefficient and refractive index maps of regions 1 to 3 shown in Fig. 2. A high-resolution image is provided as [Visualization 3](#).

Coefficient ( $TC = \sqrt{\sigma_I / \langle I \rangle}$ , with standard deviation  $\sigma$  and average  $\langle \cdot \rangle$  of the image  $I$ ) of the image gradient across all  $z$ -planes is calculated as a sharpness criterion [51]. The image gradient was obtained using a Sobel kernel of size 5 [52].

These indices serve as a measure of image sharpness, with the maximum value of the Tamura Coefficient corresponding to the best-focused image plane for a given object. Since tissue is a complex, multi-layered medium with structures located in different axial planes, multiple "sharp" planes can occur. Therefore, MATLAB's "findpeaks" function is used to identify the number and positions of these focused planes. Notice, that the Tamura Coefficient is calculated for the image gradient and not for the image. In the latter, the image is focused when the Tamura Coefficient is minimal [24].

Plot A1 displays the Tamura Coefficient of the image gradient for the DSB amplitude (blue) and digitally applied phase contrasts with  $\Gamma = 1/4\lambda$  (yellow),  $3/8\lambda$  (purple), and  $3/4\lambda$  (red). The dots indicate the maximum Tamura Coefficient for each image, with the corresponding autofocused images shown in insets A4–A7. The initial DSB amplitude is presented in inset A2, where three  $\approx 20 \mu\text{m}$  thick fiber bundles are clearly visible. Fiber bundle "1" follows a diagonal path from the lower left to the upper right, while bundle "2" is parallel but positioned in the upper left. A third bundle ("3") intersects the others at an angle of  $\approx 60^\circ$ . However, their relative depth cannot be determined from this view.

Autofocused images provide further insight into the volumetric arrangement. The DSB amplitude is focused at  $z = -22 \mu\text{m}$  (inset A4), where white arrows highlight clear boundaries between fiber bundles "1" and "3", indicating that "1" lies above "3". At  $z = 23 \mu\text{m}$  (inset A5), fiber "3" becomes more detailed (arrows), revealing regions beneath fiber "1" that were previously obscured. In addition, well-defined borders between fibers "2" and "3" suggest that fiber bundle "3" is located deeper. Inset A6, focused at  $z = -37 \mu\text{m}$ , shows detailed structures of fiber bundles "2" and "1" (arrows), supporting their position above bundle "3". Further evidence is provided by inset A7, where structures of bundle "3" appear focused at  $z = 33 \mu\text{m}$  with a phase contrast of  $\Gamma = 3/4\lambda$ , reinforcing its position below fibers "1" and "2".

Inset A3 summarizes the fiber arrangement based on the focusing depths from the previous images. Fiber "2" (green) is located at  $z \approx -30 \mu\text{m}$ , above fibers "1" ( $z \approx -20 \mu\text{m}$ ) and "3"

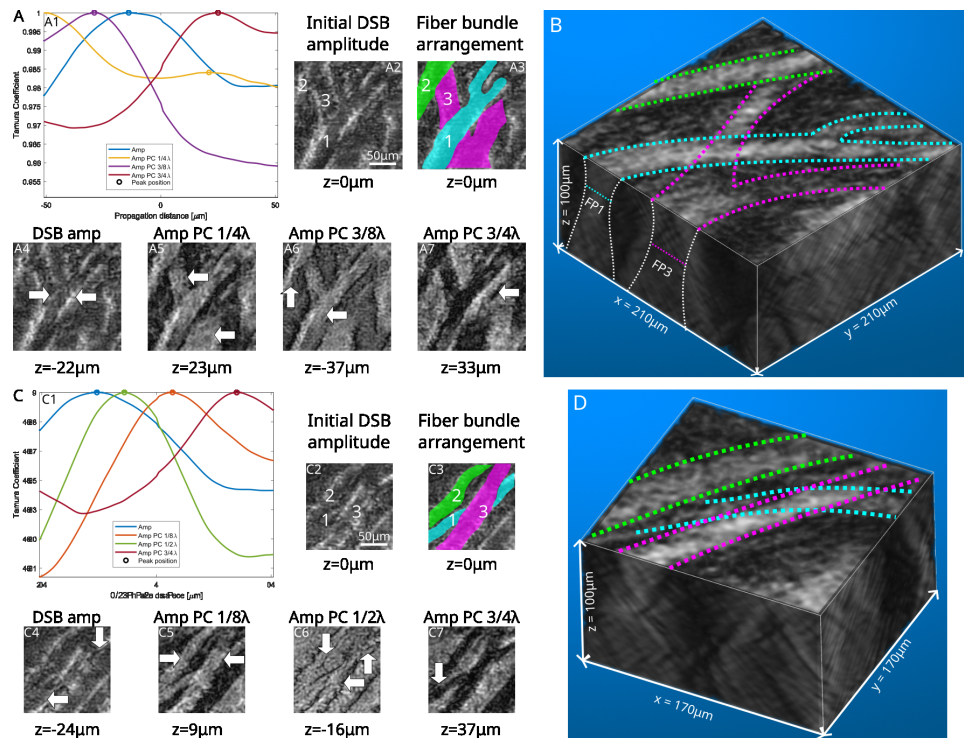


**Fig. 4.** Hologram propagation. Two fiber crossings of Region 1 in Fig. 2 are propagated from  $-50$  to  $50 \mu\text{m}$  with  $\Delta z = 1 \mu\text{m}$  in insets A2 and C2. B and D show a 3D view of the propagated volumes. The Tamura coefficient of the image gradient is plotted at each step for different digitally applied phase contrasts (A1 and C1). The images below the plots show the corresponding autofocused images at different planes (A and C 4-7). White arrows indicate landmarks that are used to resolve the arrangement of crossing fiber bundles (A3 and C3). [Visualization 4](#) and [Visualization 5](#) show videos of the propagated amplitude and applied phase contrast of  $\Gamma = 1/4$ , respectively.

( $z \approx 20 \mu\text{m}$ ). Fiber "1" (blue) crosses over fiber "3" (pink), which is a thick bundle that splits into two paths, resembling a "Y" shape. Figure 4(B) shows a 3D visualization of the propagated volume. Dashed, colored lines indicate the path of the three identified fiber bundles. The X-Z projection reveals the outlines of the fiber-bundle profiles, which form a conical structure (highlighted by white dashed lines). The focused position (FP) corresponds to the minimal extent of this cone and is marked by turquoise (bundle 1) and pink (bundle 3) dashed lines. A volumetric visualization at the focused planes of the three fiber bundles is provided in Fig. S9 in the Supplementary document. Note that the presented 3D visualization does not represent a direct reconstruction of the details of the sampled volume. Instead, it enables the 3D localization of the macroscopic fiber bundles.

The plot in Fig. 4 C1 shows the Tamura Coefficient of the image gradient for each propagated plane for the DSB amplitude (blue) and phase contrasts of  $1/8\lambda$  (orange),  $1/2\lambda$  (green), and  $3/4\lambda$  (red). The initial DSB amplitude at  $z = 0 \mu\text{m}$  (inset C2) reveals a crossing of three fiber bundles: fibers "1" and "2" run almost parallel from the bottom left to the top right, while fiber "3" crosses fiber "1" at a small angle. By evaluating the different autofocus images (insets C4-C7) and using the landmarks indicated by arrows, the fiber arrangement is reconstructed in inset C3. Fiber "1" (blue) is located below bundle "3" at  $z \approx 37 \mu\text{m}$ . Bundle "2" is located at  $z \approx 9 \mu\text{m}$ , closely followed by bundle "3" at  $z \approx -16 \mu\text{m}$ , which crosses over bundle "1". Figure 4(D) shows the

corresponding 3D visualization of the propagated volume, with dashed, colored lines indicating the trajectories of the three identified fiber bundles. A volumetric visualization at the focused planes of these fiber bundles is provided in Fig. S10 of the Supplementary Document.

## 5. Discussion

In general, the light field  $\Delta U$  can be reconstructed with high fidelity, so that different cell structures can be identified. Note also that the approximations discussed in Eqs. (11) and (12) are valid for the tissue samples: within the sample the changes in amplitude and phase are small, and smearing artifacts resulting from the Hilbert transforms (terms  $a$  and  $b$  in Eq. (7) and (9)) appear only at the interfaces between the tissue and the fixative medium (water-glycerol).

In particular, the phase images have a higher contrast and contain additional 3D information compared to the amplitude images as seen in Fig. 2. Meanwhile, the amplitude images have a high contrast at the tissue boundaries. This phenomenon is due to the fact, that the amplitude signal contains the absolute value of the Hilbert transform in Eq. (5), which is comparable to the gradient magnitude [47].

This contrast and the appearance of 3D structures in the phase images is due to the fact that the accumulated phase is measured according to Eq. (3). As a result, when one fiber overlaps another, the accumulated phase value increases compared to the surrounding areas, creating a distinguishable contrast. It is important to note that the phase images are not selective for specific biological structures within the tissue. Most label-free imaging techniques cannot resolve both cell nuclei and nerve fibers simultaneously, yet they are clearly distinguishable in the phase images. This is due to differences in the refractive index between various tissue compartments that result from their distinct biochemical compositions. For example, the myelin sheath covering nerve fibers has a higher refractive index than the cell membrane of neuronal cell bodies. Despite this difference, the phase images still allow the distinction of individual cell bodies.

Applying the darkfield filter to the recovered field  $\Delta U$  increases the signal-to-noise ratio compared to the reconstructed amplitude, because the unperturbed illumination field  $U_0$  is suppressed. This is essentially equivalent to applying a one-pixel wide high-pass filter. As a result, thick fiber bundles in Region 1 and cell bodies in Regions 2 in Fig. 2 become much easier to detect, as the dynamic range increases relative to the background.

Phase contrast can be used to provide selectively contrast for different tissue structures. For example, nerve fibers appear black at  $\Gamma = 0.75\lambda$ , while cell bodies appear bright. By adjusting the applied phase contrast in small steps, it is possible to identify specific retardance values that enhance the contrast of certain structures, which can be very useful for improving segmentation approaches. Note also the inversion of contrast in Row 4 with respect to Row 6. The same pattern applies to the unmodified amplitude image in Row 1 and the  $0.5\lambda$  retardance phase contrast image in Row 5. This behavior is due to the phase shift of the light field, described by  $\Gamma = 2\pi L/\lambda$ , meaning that the  $2\pi$  periodicity of the oscillation corresponds to a periodicity of  $1\lambda$  in retardance. Note the reduction of bright spots that appear in the images of Row 1 when the phase contrast is applied in rows 4 - 6.

The quality of the digital dark field and phase contrast images is quantified using the PSNR metric, defined as  $\text{PSNR} = 20 \log(\max(I)/\text{MSE}(I, A_{DSB}))$  where  $\max(I)$  is the maximum value of the corresponding digitally filtered image  $I$ , and MSE is the mean squared error between  $I$  and the DSB amplitude  $A_{DSB}$ . The results for each modality (dark field, DF; phase contrast, PC with a retardance of  $0.25\lambda$ ,  $0.5\lambda$ , and  $0.75\lambda$ ) for the entire sample section are presented in Table 1.

The PSNR of the dark field and phase contrast at  $0.25\lambda$  yields the highest PSNR, while the phase contrast at  $0.75\lambda$  yields the lowest. The maximum PSNR is approximately 26, while the minimum is around 12.5. These values are acceptable, considering that the contrast in the DSB amplitude images (used as a reference for the PSNR) is relatively low for some regions due to its sensitivity to tissue structure boundaries.

**Table 1. PSNR for different digital modalities of the full sample section.**  
PC: Phase contrast, DF: Dark field.

Modality	DF	PC $\lambda/4$	PC $\lambda/2$	PC $3\lambda/4$
PSNR <sub>Min</sub>	12.5	16.6	12.7	16.6
PSNR <sub>Max</sub>	22.5	26.9	21.4	25.4
$\mu$ PSNR	18.39	19.75	16.29	19.76
$\sigma$ PSNR	1.93	1.93	1.47	1.65

The attenuation coefficient in Fig. 3 covers a wide range of  $\mu_{tot} = [10 - 160] \text{ cm}^{-1}$ . For similarly prepared samples,  $\mu_{tot}$  is typically in the range  $[100 - 500] \text{ cm}^{-1}$ , while the absorption coefficient  $\mu_a$  is in the range  $[0.1 - 1] \text{ cm}^{-1}$  [53–55]. Notably, the attenuation coefficient maps closely resemble the amplitude map in Fig. 2, indicating that tissue boundaries are emphasized due to increased scattering. The refractive index maps show values of approximately  $n \approx 1.39$  for white matter and  $n \approx 1.36$  for gray matter, which are consistent with typical values obtained using comparable techniques [50,56–59]. This is due to differences in the number, thickness, and density of fibers and, consequently, varying myelin/lipid content in white or gray matter regions.

The propagation results demonstrate that the original DSB amplitude and the phase contrast amplitude focus at different axial planes, enabling the indirect, depth-resolved localization of fiber bundles. Although this method is well established, its application to dense biological specimens has been limited because holography was previously considered insufficiently coherent to resolve larger volumetric structures which tend to degrade the interference signal [27,35]. However, since the double sideband filtering technique captures the interference of the entire light field and does not require a separate reference beam, the complex field can be reconstructed with sufficient fidelity to enable numerical propagation through the sample volume. Moreover, because the refractive index of the glycerol–water ( $n_m = 1.36$ ) mounting medium closely matches that of the tissue ( $n_s \approx 1.37 - 1.42$ ), scattering and diffraction effects are minimized, resulting in higher-quality holograms. As shown above, the application of digital phase contrast highlights distinct tissue structures that are different from the DSB amplitude. Since the autofocus criterion is based on the image gradient – which corresponds to changes in image brightness – selective focusing on specific structures is achieved. In biological tissue, which is a highly inhomogeneous medium, different structures are located in varying axial planes. By applying digital phase contrast, the volumetric distribution of these structures can be analyzed and a clearer understanding of the 3D organization of the tissue can be obtained.

Due to overlapping structures, mixed phase contributions can perturb the recorded holograms and further limit axial (in-depth) resolution. Wavefront correction techniques can address these limitations and may enable the localization of structures in strongly scattering tissue, largely independent of the specific sample mounting or refractive-index–matching protocol [60].

Using the Tamura Coefficient of the gradient images yields adequate results for the autofocusing of different structures in the volume of the propagated holograms. The peaks of the metric indicate that the propagation step of  $1 \mu\text{m}$  is small enough to show significant differences in the propagated images, suggesting that changes in the 3D tissue compartment can be observed. Since the Tamura Coefficient is calculated for the entire image, a smaller image size can better extract subtle changes in sharpness, making it easier to focus on finer structures. The images evaluated have a size of  $150 \times 150$  pixels, ensuring that multiple structures are included. These structures can be focused on closely spaced planes, resulting in a broadening of the Tamura Coefficient peaks.

The DSB DHM technique is scalable to large tissue samples, as demonstrated by imaging an entire rat brain section at approximately  $3 \mu\text{m}$  lateral resolution, with an acquisition time of about 1 second per image. Only three raw images are needed per reconstruction, making the method

computationally efficient and manageable with moderate storage requirements. A non-stop, full rat brain scan comprising  $N \approx 250$  sections would require roughly one week and 100 GB of storage.

Importantly, the technique is label-free and requires no specific staining as compared to bright-field [11], fluorescence [61], or light-sheet microscopy [62]. The application of digital filters to the hologram can therefore be used to enhance the structural differentiation. Dark-field filtering improves the visibility of smaller features by suppressing background noise, while phase contrast allows for adjustable highlighting of tissue structures, supporting downstream segmentation and analysis workflows.

A key limitation of the DSB method is its sensitivity to changes in the Fourier spectrum caused by scattering or diffraction of the sample, as the filtering is performed in the Fourier plane. To maintain consistent performance, adjustment of the spatial light modulator (SLM) position is required during initial setup; once aligned, however, the system remains stable for a full brain section. Furthermore, the reconstruction of the optical field is not exact due to the contributions that originate from the convolution  $R$  in Eq. (6). While phase-step common-path interferometry could potentially reduce these artifacts, such approaches generally exhibit reduced robustness to variations in the Fourier spectrum [20].

## 6. Conclusion

This work demonstrates that DSB-based holographic techniques offer a powerful, efficient and scalable approach to multimodal label-free 3D tissue imaging under certain conditions that suppress scattering and diffraction effects, such as refractive-index matching between the prepared tissue and the surrounding medium, as well as mounting the sample between glass slides to reduce surface roughness. It has the potential to advance histological analysis, particularly in disentangling complex fiber architectures. It can be used as a stand-alone tool, or complemented with existing techniques that rely on the same tissue preparation, such as polarized light imaging or scattered light imaging. In particular, this method enables the indirect localization of fiber pathways within the sample volume, achieving an axial localization precision of  $\approx 1\mu\text{m}$ . Additionally, the calculation of the refractive index facilitates the investigation of myelin distribution at a lateral resolution of  $\approx 3\mu\text{m}$ . The application of digital Fourier filters further enhances contrast, improving the differentiation of tissue structures within the volume. These features closely align with the need for high-resolution volumetric imaging to characterize complex sample morphologies more effectively. Furthermore, this work opens the door to investigating more complex 3D structures with digital holographic microscopy, particularly in the context of strongly scattering samples.

**Funding.** HORIZON EUROPE Framework Programme (No. 101147319); Commissariat à l'Énergie Atomique et aux Énergies Alternatives (AIDAS); Dirección General de Asuntos del Personal Académico, Universidad Nacional Autónoma de México (IN104924); John Templeton Foundation (62220).

**Acknowledgments.** Special thanks to the lab team of INM-1 for preparing the rat brain samples, with particular appreciation to Anna Steffens, Phillip Schlömer, and Markus Cremer. Generative AI was used for spelling and grammar correction.

**Disclosures.** The authors declare no conflict of interest.

**Data availability.** Data from the simulations can be found in Ref. [39]. Further data underlying the results presented in this article may be obtained from the corresponding author upon reasonable request.

**Supplemental document.** See [Supplement 1](#) for supporting content.

## References

1. M. Axer and K. Amunts, "Scale matters: The nested human connectome," *Science* **378**(6619), 500–504 (2022).
2. I. Costantini, M. Axer, C. Magnain, *et al.*, "Editorial: The human brain multiscale imaging challenge," *Front. Neuroanat.* **16**, 1060405 (2022).

3. Z. Zheng, J. S. Lauritzen, E. Perlman, *et al.*, “A complete electron microscopy volume of the brain of adult drosophila melanogaster,” *Cell* **174**(3), 730–743.e22 (2018).
4. S. J. Cook, T. A. Jarrell, C. A. Brittin, *et al.*, “Whole-animal connectomes of both caenorhabditis elegans sexes,” *Nature* **571**(7763), 63–71 (2019).
5. E. Van Reeth, I. W. K. Tham, C. H. Tan, *et al.*, “Super-resolution in magnetic resonance imaging: A review,” *Concepts Magn. Reson. Part A* **40A**(6), 306–325 (2012).
6. A. Mukhatov, T.-A. Le, T. T. Pham, *et al.*, “A comprehensive review on magnetic imaging techniques for biomedical applications,” *Nano Sel.* **4**(3), 213–230 (2023).
7. C. Xu, M. Nedergaard, D. J. Fowell, *et al.*, “Multiphoton fluorescence microscopy for in-vivo imaging,” *Cell* **187**(17), 4458–4487 (2024).
8. H. Wang, C. Magnain, R. Wang, *et al.*, “as-psoct: Volumetric microscopic imaging of human brain architecture and connectivity,” *NeuroImage* **165**, 56–68 (2018).
9. M. Axer, D. Graessel, M. Kleiner, *et al.*, “High-resolution fiber tract reconstruction in the human brain by means of three-dimensional polarized light imaging,” *Front. Neuroinform.* **5**, 00034 (2011).
10. M. Koike-Tani, T. Tani, S. B. Mehta, *et al.*, “Polarized light microscopy in reproductive and developmental biology,” *Mol. Reproduction Dev.* **82**(7–8), 548–562 (2015).
11. H. Al.Turkistani, F. Tashkandi, and Z. Mohammedsaleh, “Histological stains: A literature review and case study,” *Glob. J. Health Sci.* **8**(3), 72–79 (2015).
12. B. Ghosh and K. Agarwal, “Viewing life without labels under optical microscopes,” *Communications Biology* (2023).
13. F. Darzi and T. Bocklitz, “A review of medical image registration for different modalities,” *Bioeng.* **11**(8), 786 (2024).
14. P. F. Gao, G. Lei, and C. Z. Huang, “Dark-field microscopy: Recent advances in accurate analysis and emerging applications,” *Anal. Chem.* **93**(11), 4707–4726 (2021).
15. E. V. Yakovlev, I. V. Simkin, A. A. Shirokova, *et al.*, “Machine learning approach for recognition and morphological analysis of isolated astrocytes in phase contrast microscopy,” *Sci. Rep.* **14**(1), 9846 (2024). PMID: 33620210.
16. P. D. Martel, C. Zhang, A. A. Linninger, *et al.*, “Phase contrast reflectance confocal brain imaging at 1650 nm,” *J. Biomed. Opt.* **29**(2), 026501 (2024).
17. M. Menzel, J. A. Reuter, D. Gräbel, *et al.*, “Scattered light imaging: Resolving the substructure of nerve fiber crossings in whole brain sections with micrometer resolution,” *NeuroImage* **233**, 117952 (2021).
18. F.-C. Yeh, A. Irimia, D. C. de Almeida Bastos, *et al.*, “Tractography methods and findings in brain tumors and traumatic brain injury,” *NeuroImage* **245**, 118651 (2021).
19. B. Jeurissen, M. Descoteaux, S. Mori, *et al.*, “Diffusion mri fiber tractography of the brain,” *NMR Biomed.* **32**(4), e3785 (2019). E3785 NBM-17-0045.R2.
20. X. Quan, D. Kato, V. Daria, *et al.*, “Holographic microscope and its biological application,” *Neurosci. Res.* **179**, 57–64 (2022). Lighting up cosmic neuronal networks with transformative in vivo calcium imaging.
21. Y. Park, C. D. Depeursinge, and G. Popescu, “Quantitative phase imaging in biomedicine,” *Nat. Photonics* **12**(10), 578–589 (2018).
22. Z. Huang and L. Cao, “Quantitative phase imaging based on holography: trends and new perspectives,” *Light: Sci. Appl.* **13**(1), 145 (2024).
23. J. Gao, J. A. Lyon, D. P. Szeto, *et al.*, “In vivo imaging and quantitative analysis of zebrafish embryos by digital holographic microscopy,” *Biomed. Opt. Express* **3**(10), 2623–2635 (2012).
24. C. Ramirez, I. Estevez, A. Lizana, *et al.*, “Analysis of the image magnification produced by inline holographic systems based on the double-sideband filter,” *Appl. Sci.* **14**(12), 5118 (2024).
25. P. Shamshirpour, M. Rahnama, M. Nikoobakht, *et al.*, “A dynamic study of vegf-a sidox-evs trafficking through the in-vitro insert co-culture blood-brain barrier model by digital holographic microscopy,” *Front. Oncol.* **14**, 1292083 (2024).
26. L. M. Rooney, L. S. Kölln, R. Scrimgeour, *et al.*, “Three-dimensional observations of an aperiodic oscillatory gliding behavior in myxococcus xanthus using confocal interference reflection microscopy,” *mSphere* **5**(1), 1 (2020).
27. X. Hua, K. Han, B. Mandracchia, *et al.*, “Light-field flow cytometry for high-resolution, volumetric and multiparametric 3d single-cell analysis,” *Nat. Commun.* **15**(1), 1975 (2024).
28. T. Nguyen, M. Kandel, M. Rubessa, *et al.*, “Gradient light interference microscopy for 3d imaging of unlabeled specimens,” *Nat. Commun.* **8**(1), 210 (2017).
29. R. M. Abdelazeem, D. Youssef, J. El-Azab, *et al.*, “Three-dimensional holographic reconstruction of brain tissue based on convolution propagation,” *J. Phys.: Conf. Ser.* **1472**(1), 012008 (2020).
30. V. V. Senatorov, “Dark-field microscopy visualization of unstained axonal pathways using oil of wintergreen,” *J. Neurosci. Methods* **113**(1), 59–62 (2002).
31. E. Min, M. E. Kandel, C. J. Ko, *et al.*, “Label-free, multi-scale imaging of ex-vivo mouse brain using spatial light interference microscopy,” *Sci. Rep.* **6**(1), 39667 (2016).
32. F. Verpillat, F. Joud, P. Desbiolles, *et al.*, “Dark-field digital holographic microscopy for 3d-tracking of gold nanoparticles,” *Opt. Express* **19**(27), 26044–26055 (2011).
33. N. Lue, W. Choi, G. Popescu, *et al.*, “Quantitative phase imaging of live cells using fast fourier phase microscopy,” *Appl. Opt.* **46**(10), 1836–1842 (2007).
34. G. Kim, H. Hugonnet, K. Kim, *et al.*, “Holotomography,” *Nat. Rev. Methods Primers* **4**(1), 51 (2024). Publisher Copyright: © Springer Nature Limited 2024.

35. M. K. Kim, "Principles and techniques of digital holographic microscopy," *SPIE Rev.* **1**(1), 018005 (2010).
36. V. Micó, Z. Zalevsky, and J. Garcia, "Superresolved common-path phase-shifting digital inline holographic microscopy using a spatial light modulator," *Opt. Lett.* **37**(23), 4988–4990 (2012).
37. J. Kim and S. Lee, "Digital in-line holographic microscopy for label-free identification and tracking of biological cells," *Mil. Med. Res.* **11**(1), 38 (2024).
38. A. E. G. Madsen, M. A. Panah, P. E. Larsen, *et al.*, "On-axis digital holographic microscopy: Current trends and algorithms," *Opt. Commun.* **537**, 129458 (2023).
39. C. Ramirez, A. Lizana, C. Iemmi, *et al.*, "Inline digital holographic movie based on a double-sideband filter," *Opt. Lett.* **40**(17), 4142–4145 (2015).
40. D. Scheidt, "Replication data for the article "Exploring the 3D Architecture of Rat Brain Tissue Using Digital Holographic Microscopy"," (2025).
41. M. Stacho, C. Herold, N. Rook, *et al.*, "A cortex-like canonical circuit in the avian forebrain," *Science* **369**(6511), eabc5534 (2020).
42. S. Preibisch, S. Saalfeld, and P. Tomancak, "Globally optimal stitching of tiled 3d microscopic image acquisitions," *Bioinformatics* **25**(11), 1463–1465 (2009).
43. T. Latychevskaia and H.-W. Fink, "Practical algorithms for simulation and reconstruction of digital in-line holograms," *Appl. Opt.* **54**(9), 2424–2434 (2015).
44. L. Ma, H. Wang, Y. Li, *et al.*, "Numerical reconstruction of digital holograms for three-dimensional shape measurement," *J. Opt. A: Pure Appl. Opt.* **6**(4), 396–400 (2004).
45. Á. Barroso, S. Ketelhut, P. Heiduschka, *et al.*, "Hyperspectral digital holographic microscopy approach for reduction of coherence induced disturbances in quantitative phase imaging of biological specimens," in *Speckle 2018: VII International Conference on Speckle Metrology*, vol. 10834 M. Kujawinska and L. R. Jaroszewicz, eds., International Society for Optics and Photonics (SPIE, 2018), p. 108340I.
46. C. Ramirez, A. Lizana, C. Iemmi, *et al.*, "Method based on the double sideband technique for the dynamic tracking of micrometric particles," *J. Opt.* **18**(6), 065603 (2016).
47. D. Hilbert, *Grundzüge einer allgemeinen Theorie der linearen Integralgleichungen* (Chelsea Publishing Company, 1953). Originally published by B.G. Teubner in 1912. This is a reprint edition.
48. E. A. Papp, T. B. Leergaard, E. Calabrese, *et al.*, "Waxholm space atlas of the sprague dawley rat brain," *NeuroImage* **97**, 374–386 (2014).
49. M. A. Herráez, D. R. Burton, M. J. Lalor, *et al.*, "Fast two-dimensional phase-unwrapping algorithm based on sorting by reliability following a noncontinuous path," *Appl. Opt.* **41**(35), 7437–7444 (2002).
50. B. Rappaz, P. Marquet, E. Cuche, *et al.*, "Measurement of the integral refractive index and dynamic cell morphometry of living cells with digital holographic microscopy," *Opt. Express* **13**(23), 9361–9373 (2005).
51. Y. Zhang, H. Wang, Y. Wu, *et al.*, "Edge sparsity criterion for robust holographic autofocusing," *Opt. Lett.* **42**(19), 3824–3827 (2017).
52. K. N. Kumar, G. L. N. V. Kartheek, and G. V. S. C. S. L. V. Prasad, "Image segmentation using extended edge operator for mammographic images," *J. Sci. & Technol. (JST)* **6**(6), 174–179 (2021).
53. R. Marchesini, A. Bertoni, S. Andreola, *et al.*, "Extinction and absorption coefficients and scattering phase functions of human tissues in vitro," *Appl. Opt.* **28**(12), 2318–2324 (1989).
54. I. Driver, C. P. Lowdell, and D. V. Ash, "In vivo measurement of the optical interaction coefficients of human tumours at 630 nm," *Phys. Med. Biol.* **36**(6), 805–813 (1991).
55. J. Shapey, Y. Xie, E. Nabavi, *et al.*, "Optical properties of human brain and tumour tissue: An ex vivo study spanning the visible range to beyond the second near-infrared window," *J. Biophotonics* **15**(4), e202100072 (2022).
56. L. Khurana, D. Keppeler, L. Jablonski, *et al.*, "Model-based prediction of optogenetic sound encoding in the human cochlea by future optical cochlear implants," *Comput. Struct. Biotechnol. J.* **20**, 3621–3629 (2022).
57. S. L. Jacques, "Optical properties of biological tissues: a review," *Phys. Med. Biol.* **58**(11), R37–R61 (2013).
58. A. J. Lee, H. Hugonnet, Y. S. Kim, *et al.*, "Volumetric refractive index measurement and quantitative density analysis of mouse brain tissue with sub-micrometer spatial resolution," *Adv. Photonics Res.* **4**(10), 2300112 (2023).
59. J. Sun, S. J. Lee, L. Wu, *et al.*, "Refractive index measurement of acute rat brain tissue slices using optical coherence tomography," *Opt. Express* **20**(2), 1084–1095 (2012).
60. V. Balasubramani, H.-Y. Tu, X. J. Lai, *et al.*, "Adaptive wavefront correction structured illumination holographic tomography," *Sci. Rep.* **9**(1), 10489 (2019).
61. J. Simpson and P. C. Hawes, *Preparation of Immunofluorescently Labeled Tissue Sections for Imaging at Low and High Magnifications in the Confocal Microscope* (Springer US, 2022), pp. 51–61.
62. P. Ariel, "A beginner's guide to tissue clearing," *The Int. J. Biochem. & Cell Biol.* **84**, 35–39 (2017).